Photoacoustics 32 (2023) 100543

Contents lists available at ScienceDirect

Photoacoustics

journal homepage: www.elsevier.com/locate/pacs

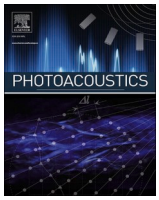

Adaptive polarization photoacoustic computed tomography for biological anisotropic tissue imaging

Yang Zhang [a], Christ Glorieux [b], Shufan Yang [c], Kai Gu [a], Zhiying Xia [a], Ruijie Hou [a], Lianping Hou [d], Xuefeng Liu [a,*], Jichuan Xiong [a,*]

[a] School of Electronic and Optical Engineering, Nanjing University of Science and Technology, Nanjing 210094, China
[b] Laboratory for Soft Matter and Biophysics, Department of Physics and Astronomy, KU Leuven, Leuven B-3001, Belgium
[c] School of Computing, Edinburgh Napier University, Edinburgh, Scotland EH10 5DT, UK
[d] James Watt School of Engineering, University of Glasgow, Glasgow G12 8QQ, UK

ARTICLE INFO

Keywords:
Photoacoustic computed tomography
Polarized light
Adaptive
Anisotropic tissue

ABSTRACT

Most photoacoustic computed tomography (PACT) systems usually ignore the anisotropy of the tissue absorption coefficient, which will lead to the lack of information in reconstructed images. In this work, the effect is addressed of the possible optical absorption anisotropy of tissue on PACT images. The functional relationship is derived between the photoacoustic response and the polarization angle of the excitation light. An adaptive polarized light photoacoustic imaging (AP-PACT) approach is proposed and shown to make up for the lack of imaging information and achieve optimal image contrast when imaging samples with anisotropic optical absorption, by utilizing the standard deviation of photoacoustic response as the feedback signal in an adaptive data acquisition process. The method is implemented both on phantom and in vitro experiments, which show that AP-PACT can recover anisotropic absorption-related information from reconstructed images and thus significantly improve their quality.

1. Introduction

Photoacoustic computed tomography (PACT) combines the advantages of optical imaging with high contrast and low scattering ultrasound imaging and utilizes the absorption of light by tissues to realize deep imaging with a high spatial resolution of biological tissues [1–3]. At present, most PACT systems ignore the possible dependence of the optical absorption of tissues on the polarization state of the excitation light and use non-polarized light or light with unknown polarization to excite photoacoustic (PA) signals. However, optical absorption anisotropy is a characteristic that exists in many biological tissues [4–6]. It is often closely related to the structural and functional properties of samples like the fiber bundle structure of muscles [7] and the tubular microstructure of dentin [8]. Hence, variations in the polarization of the excitation light that reaches different regions, caused by to uncontrolled light source polarization or scattering-induced polarization changes, may lead to artifacts and information loss in PACT images [9].

Contrary to optical imaging and characterization methods of biological tissues, where effects of optical anisotropy have been investigated both theoretically and experimentally [4,10,11], studies on their impact on conventional PACT are scarce. The concept of polarization-sensitive photoacoustic tomography was first proposed by Razansky et al. [12]. In their experimental work, anisotropic effects in photoacoustic signals were detected in diffusive media. Since their work, several studies addressing the anisotropic absorption of tissues, e.g. to visualize the anisotropy of the target, have been reported [13–17]. A dichroism-sensitive PACT method was proposed by Qu et al. [13], which can determine the orientation of the optical axis of uniaxial dichroic tissues. In this method, the Fourier transform of PA amplitude is calculated pixel by pixel by locking the polarization modulation frequency. The amount of calculation is extremely large and uneven imaging may be caused.

Also polarized optical resolution photoacoustic microscopy (OR-PAM) has been implemented to visualize the anisotropy of samples [14–16]. Hu et al. [14] applied polarized light to OR-PAM for the first time; Zhang et al. [15] proposed an imaging method that can quantify the anisotropy of the target; Zhou et al. [16] divided a laser beam into three beams, so that linear dichroism could be measured in a single shot.

* Corresponding authors.
E-mail addresses: xuefeng_liu@njust.edu.cn (X. Liu), jichuan.xiong@njust.edu.cn (J. Xiong).

https://doi.org/10.1016/j.pacs.2023.100543
Received 1 June 2023; Received in revised form 6 August 2023; Accepted 8 August 2023
Available online 9 August 2023

However, compared to PACT, OR-PAM imaging mode has the limitations of a small field of view, shallow imaging depth, and slow imaging speed. In a word, the reported photoacoustic imaging based on anisotropy is an extension of photoacoustic imaging, which does not solve the problem of imaging information loss. Furthermore, to date there is no comprehensive theoretical description of polarization PA imaging.

In this work, we address the above mentioned issues. First, we derive a general theoretical model of PA response for a given polarization angle of the excitation light from the Maxwell equations. Next, we propose an adaptive polarization PACT (AP-PACT) method. The method use the standard deviation (σ_P) value of the PA signals as feedback signal, which can optimize the quality of PA signals in real-time and compensates for the possible information loss of the orientation of the optical axis in optically anisotropic samples, thus avoids the degradation of images that occurs in conventional PACT by ignoring the orientation of the optical axis in tissue. Finally, the method is verified in vitro by imaging chicken heart tissue and bovine tendon tissue embedded in a scattering medium.

2. Method

2.1. Optical absorption and photoacoustic signals in an optically anisotropic medium

It is well known that in an isotropic medium, the electric displacement **D**, the electric field **E**, and the dielectric constant ε obey the relation $\boldsymbol{D} = \varepsilon \boldsymbol{E}$. In this paper, an anisotropy homogeneous medium is considered, in which each component of D is linearly related to the different components of E.

$$\left.\begin{array}{l} D_x = \varepsilon_{xx}E_x + \varepsilon_{xy}E_y + \varepsilon_{xz}E_z \\ D_y = \varepsilon_{yx}E_x + \varepsilon_{yy}E_y + \varepsilon_{yz}E_z \\ D_z = \varepsilon_{zx}E_x + \varepsilon_{zy}E_y + \varepsilon_{zz}E_z \end{array}\right\} \tag{1}$$

where the nine quantities ε_{xx}, ε_{xy}, …, ε_{zz} are constants of the medium, and constitute the dielectric tensor; thus the vector D is the product of this tensor with E.

For simplicity, we assume a system of coordinate axes coincident with the principal dielectric axes. Eq. (1) is then induced to the simpler Eq. (2).

$$D_x = \varepsilon_x E_x \ , \ D_y = \varepsilon_y E_y \ , \ D_z = \varepsilon_z E_z \tag{2}$$

Where ε_x, ε_y, ε_z are the principal dielectric constants. Eq. (2) indicates that in general the vectors **D** and **E** in an anisotropic medium have different directions, unless **E** is oriented along one of the principal axes.

Two of Maxwell's equations in differential form, for a region that does not carry currents are

$$\nabla \times \boldsymbol{H} - \frac{\partial \boldsymbol{D}}{\partial t} = 0, \nabla \times \boldsymbol{E} + \frac{\partial \boldsymbol{B}}{\partial t} = 0 \tag{3}$$

where in the frequency domain the operation $\partial/\partial t$ is equivalent to multiplication by $-i\omega$, while the Hamilton operator ∇ is equivalent to multiplication by $i\omega n s_x/c$ ($\omega = 2\pi\nu$ is the angular frequency, c/n is the speed of sound in the medium in the direction of the unit wave-normal $\boldsymbol{s}$). c is the speed of light in a vacuum and n is the refractive index. Then, Eq. (3) becomes

$$n\boldsymbol{s} \times \boldsymbol{H} = -\boldsymbol{D}, n\boldsymbol{s} \times \boldsymbol{E} = \mu \boldsymbol{H} \tag{4}$$

with $\boldsymbol{B} = \mu_0 \boldsymbol{H}$. $\boldsymbol{B}$, $\boldsymbol{H}$ and μ_0 are the magnetic flux density, the magnetic field vector and the permeability of vacuum, respectively. Eliminating $\boldsymbol{H}$ between Eq. (4) and using the well-known vector identity $[\boldsymbol{a} \times (\boldsymbol{b} \times \boldsymbol{c}) = (\boldsymbol{a}\cdot\boldsymbol{c})\boldsymbol{b} - (\boldsymbol{a}\cdot\boldsymbol{b})\boldsymbol{c}]$, we obtain

$$\boldsymbol{D} = -\frac{n^2}{\mu_0}\boldsymbol{s} \times (\boldsymbol{s} \times \boldsymbol{E}) = \frac{n^2}{\mu_0}[\boldsymbol{E} - (\boldsymbol{s} \bullet \boldsymbol{E})\boldsymbol{s}] \tag{5}$$

Substitution Eq. (2) into $\boldsymbol{D}(D_x, D_y, D_z)$ in Eq. (5) gives

$$\mu_0 \varepsilon_k E_k = n^2[E_k - (\boldsymbol{E}\cdot\boldsymbol{s})s_k], (k = x, y, z) \tag{6}$$

As the set of equations in E_x, E_y, E_z in Eq. (6) is linear and homogeneous, it can be satisfied by non-zero values of these components only if the associated determinant vanishes. This implies that a certain relation must be satisfied by the refractive index n, the vector $\boldsymbol{s}(s_x, s_y, s_z)$ and the principal dielectric constants $\varepsilon_x, \varepsilon_y, \varepsilon_z$. This relation may be derived by rewriting Eq. (6) as follows:

$$E_k = \frac{n^2 s_k(\boldsymbol{E}\cdot\boldsymbol{s})}{n^2 - \mu_0 \varepsilon_k} \tag{7}$$

Multiplying it by s_k and adding the resulting three equations ($k = x,y,z$); dividing the expression which then results by the common factor $\boldsymbol{E}\cdot\boldsymbol{s}$, we obtain

$$\frac{{s_x}^2}{n^2 - \mu_0 \varepsilon_x} + \frac{{s_y}^2}{n^2 - \mu_0 \varepsilon_y} + \frac{{s_z}^2}{n^2 - \mu_0 \varepsilon_z} = \frac{1}{n^2} \tag{8}$$

This equation may be expressed in a slightly different form. We multiply both sides by n^2 and subtract ${s_x}^2 + {s_y}^2 + {s_z}^2 = 1$. Next, we multiply the resulting expression by $-n^2$ and find that

$$\frac{{s_x}^2}{\frac{1}{n^2} - \frac{1}{\mu_0 \varepsilon_x}} + \frac{{s_y}^2}{\frac{1}{n^2} - \frac{1}{\mu_0 \varepsilon_y}} + \frac{{s_z}^2}{\frac{1}{n^2} - \frac{1}{\mu_0 \varepsilon_z}} = 0 \tag{9}$$

We define three principal velocities of propagation by the formulae. Note that v_x, v_y and v_z are not components of a vector and are defined only with reference to the principal axes of the medium.

$$v_x = \frac{c}{\sqrt{\mu_0 \varepsilon_x}}, v_x = \frac{c}{\sqrt{\mu_0 \varepsilon_y}}, v_x = \frac{c}{\sqrt{\mu_0 \varepsilon_z}} \tag{10}$$

When the expression $v_p = c/n$ is used for the phase velocity v_p of the electromagnetic wave, then by substituting Eq. (10) into Eq. (9), we obtain

$${s_x}^2\left({v_p}^2 - {v_y}^2\right)\left({v_p}^2 - {v_z}^2\right) + {s_y}^2\left({v_p}^2 - {v_z}^2\right)\left({v_p}^2 - {v_x}^2\right) +$$

$${s_z}^2\left({v_p}^2 - {v_x}^2\right)\left({v_p}^2 - {v_y}^2\right) = 0 \tag{11}$$

In our study, the media are assumed to be uniaxial, with their optical axes in the z-direction, $v_x = v_y$. Let v_o denote the common velocity and v_e in place of v_z, thus Eq. (11) is induced to

$$\left({v_p}^2 - {v_o}^2\right)\left[\left({s_x}^2 + {s_y}^2\right)\left({v_p}^2 - {v_e}^2\right) + {s_z}^2\left({v_p}^2 - {v_o}^2\right)\right] = 0 \tag{12}$$

Let ϑ denote the angle that the wave normal $\boldsymbol{s}$ makes with the z-axis; then ${s_x}^2 + {s_y}^2 = \sin^2\vartheta$, ${s_z}^2 = \cos^2\vartheta$, and Eq. (12) becomes

$$\left({v_p}^2 - {v_o}^2\right)\left[\left({v_p}^2 - {v_e}^2\right)\sin^2\vartheta + \left({v_p}^2 - {v_o}^2\right)\cos^2\vartheta\right] = 0 \tag{13}$$

The two roots of this equation ($v_p^{'}$ and $v_p^{'}$ say) are given by

$$\begin{cases} {v_p^{'}}^2 = {v_o}^2 \\ {v_p^{"}}^2 = {v_o}^2\cos^2\vartheta + {v_e}^2\sin^2\vartheta \end{cases} \tag{14}$$

Taking into account the absorption of uniaxial anisotropic media, the form of Eq. (14) is converted into

$$\begin{cases} {\widehat{v}_p^{'}}^2 = {\widehat{v}_o}^2 \\ {\widehat{v}_p^{"}}^2 = {\widehat{v}_o}^2\cos^2\vartheta + {\widehat{v}_e}^2\sin^2\vartheta \end{cases} \tag{15}$$

For simplicity of calculation, the second power of the attenuation index κ may be neglected in comparison with unity. We may therefore write

$$\widehat{v}_p = v_p(1 - i\kappa) \text{and} {\widehat{v}_p}^2 = {v_p}^2(1 - 2i\kappa) \tag{16}$$

According to Eq. (15) and Eq. (16), we obtain

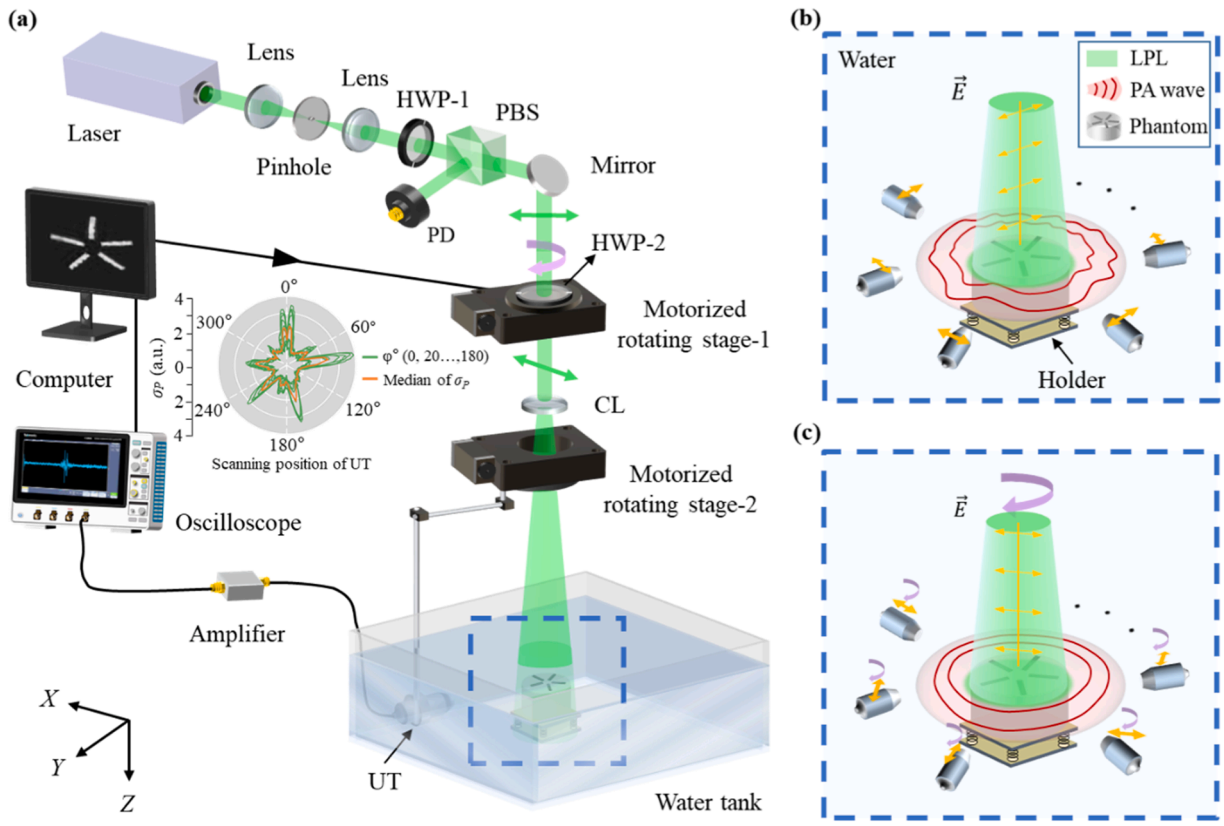

Fig. 1. System schematic of AP-PACT. (a) Experimental system diagram. Radar chart: The computer calculates the 10 σ_P values (green) and their median value (orange) in real time. HWP: half-wave plate; PBS: polarization beam splitter; PD: photodiode; CL: concave lens; UT: ultrasonic transducer. (b) In conventional PACT, the UT collect PA signals excited by polarized light in the same direction at each position (0–360° in steps of 1°). LPL: linearly polarized light; PA: photoacoustic. (c) In the proposed approach (AP-PACT) (a and c), for each UT orientation, PA signals are adaptively collected, according to the σ_P value of PA signals excited by 10 different polarization angles.

$$v_p^{"2}(1-2i\kappa_p) = v_o^2(1-2i\kappa_o)\cos^2\vartheta + v_e^2(1-2i\kappa_e)\sin^2\vartheta \tag{17}$$

Eq. (17) can be decomposed into the following two factors.

$$v_p^{"2} = v_o^2\cos^2\vartheta + v_e^2\sin^2\vartheta, \kappa_p^{"}v_p^{"2} = \kappa_o v_o^2\cos^2\vartheta + \kappa_e v_e^2\sin^2\vartheta \tag{18}$$

According to the propagation property of wave in a conductor: $\alpha = 2n\kappa\omega/c$, where α is the absorption coefficient, by substituting it into Eq. (18), we obtain

$$\alpha_p = \alpha_o\frac{n_p^3}{n_o^3}\cos^2\vartheta + \alpha_e\frac{n_p^3}{n_e^3}\sin^2\vartheta \tag{19}$$

In Eq.(19) $\alpha_o$is the absorption coefficient for light polarized perpendicular to the optical axis of the tissue material while α_e is the one for light polarized parallel with the optical axis.

In PACT, the PA amplitude $p_0(\vec{r},\varphi)$ can be represented as the product of the optical absorption coefficient $\alpha(\vec{r},\varphi)$ of the biological tissue and the local light fluence $F(\vec{r},\varphi)$ [17].

$$p_0(\vec{r},\varphi)\propto\alpha(\vec{r},\varphi)F(\vec{r},\varphi) \tag{20}$$

where $\vec{r}$ is the spatial position and φ represents the polarization angle of excitation light.

Substituting Eq. (19) into Eq. (20) yields

$$p_0(\vec{r},\varphi)\propto\left[\alpha_o(\vec{r})\frac{n_p^3(\vec{r},\varphi)}{n_o^3(\vec{r})}\cos^2(\varphi-\vartheta(\vec{r}))+\right.$$

$$\left.\alpha_e(\vec{r})\frac{n_p^3(\vec{r},\varphi)}{n_e^3(\vec{r})}\sin^2(\varphi-\vartheta(\vec{r}))\right]F(\vec{r},\varphi) \tag{21}$$

Since the refractive index of changes very weakly in many anisotropic tissues, we assume here that $n_p(\vec{r},\varphi)\approx n_0(\vec{r})\approx n_e(\vec{r})$ and $F(\vec{r},\varphi)\approx F(\vec{r})$, Eq. (21) is reduced to

$$p_0(\vec{r},\varphi)\propto\left[\frac{\alpha_o(\vec{r})+\alpha_e(\vec{r})}{2}+\frac{\alpha_o(\vec{r})-\alpha_e(\vec{r})}{2}\cos2(\varphi-\vartheta(\vec{r}))\right]F(\vec{r}) \tag{22}$$

Clearly, the local PA signal magnitude depends on the angle between the electric field vector and the local optical axis. However, for anisotropic tissues, it is difficult to directly detect the polarization information of tissues because the excitation light gets depolarized as it penetrates deeper (see Supplementary information). Therefore, we propose to use the standard deviation value (σ_P) of PA signal to construct the relationship between the polarization angle of excitation light and PA response.

$$\sigma_P = \sqrt{\frac{\sum_{i=1}^{N_t}[p_d(\vec{r}_0,t_i,\varphi)-\overline{p_d(\vec{r}_0,t,\varphi)}]^2}{N_t-1}} \tag{23}$$

Where p_d is the detected PA signal, $\overline{p_d}$ is the average of p_d, N_t is the number of samples in a PA time-domain response. Here, the sampling time was 16 ns and $N_t = 4000$.

2.2. AP-PACT approach

Fig. 1(a) shows the scheme of the proposed AP-PACT system, which consists of three major subsystems: an optical system, an adaptive data acquisition system, and an image reconstruction system.

The optical system is composed of a laser system and a beam-shaping

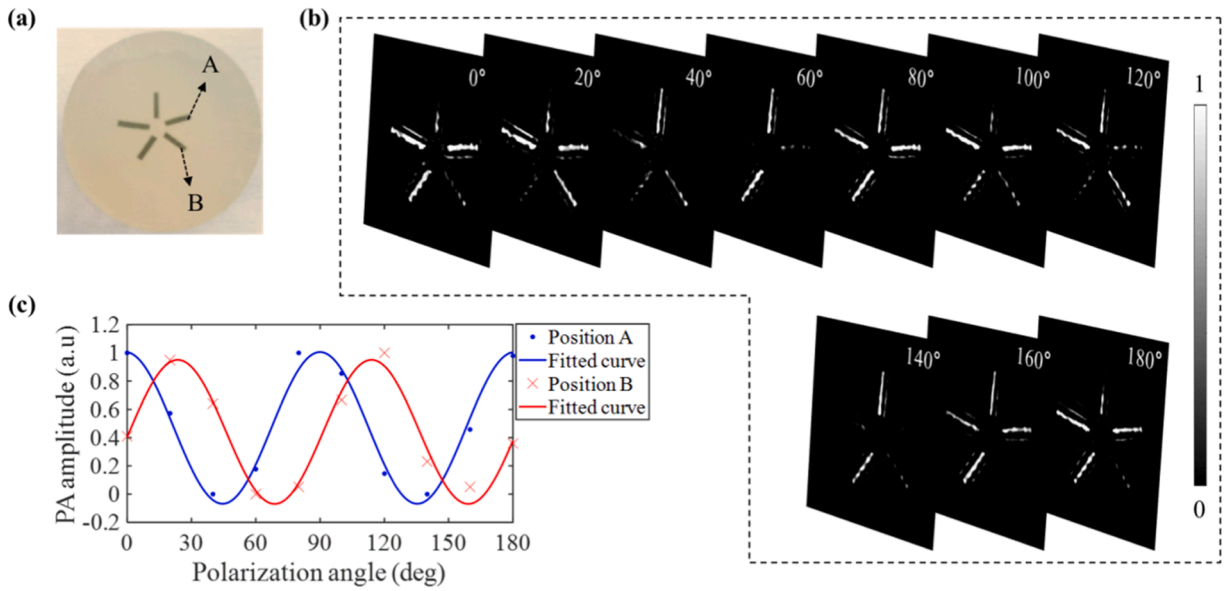

Fig. 2. Influence of polarization orientation on reconstruct image. (a) Photograph of the phantom. (b) Experimentally obtained PA images obtained for 10 polarization angles. (c) PA image magnitude values of the reconstructed PA image versus polarization angle at locations A and B, and best fitting sinusoidal curves.

system. A 532 nm wavelength pulsed laser (TINY-200L, Grace; 10 Hz repetition rate and 5 ns pulse width) was used as optical excitation source. The laser beam was first spatially filtered and expanded by a pinhole and two lenses. The expanded beam passed through a half-wave plate-1 (HWP-1) and a polarizing beam splitter. By rotating the HWP-1, the laser energy delivered to the object could be adjusted. After passing through the PBS, a small fraction of the energy beam was reflected onto a photodiode to monitor the laser intensity, and after passing through a rotating mirror, the other beam was sent through half-wave plate-2 (HWP-2) to rotate the initially vertical polarization to a desired orientation. A concave lens then expanded the incident light to a diameter of ~ 2.5 cm onto the sample surface.

The adaptive data acquisition system consisted of an adaptive polarization-rotating light stage (consisting of an HWP-2 fixed on the motorized rotating stage-1), an ultrasound transducer (fixed on the motorized rotating stage-2) and a data acquisition system. The motorized rotating stage-1 rotated the HWP-2 so that the polarization angle of the excitation light before entering the scattering medium was scanned from 0° to 180° in 10 steps of 20°. Here the PA signal was detected by a modified ultrasonic transducer (Doppler Inc., 10 mm element size, 5 MHz central frequency, and 79 % bandwidth at − 6 dB) with a diameter of 2 mm on the receiving surface to increase the receiving angle of the PA signal [18]. The signal was amplified by a 26 dB low-noise pre-amplifier (ZFL-500LN, Mini-Circuits) and recorded by an oscilloscope (MSO46, Tektronix), which transferred the digitized signal to a personal computer (PC).

In the radar chart in Fig. 1(a), the 10 green curves represent the calculated σ_P values. The orange curve represents the median σ_P values. In conventional PACT, the ultrasonic transducer (UT) collects PA waves generated for a fixed polarization direction of the excitation light, as shown in Fig. 1(b). With the proposed AP-PACT method, the UT adaptively selects (AS) the PA signals corresponding to the median σ_P value for each scanning position, as shown in Fig. 1(c).

The image reconstruction was done by a filtered back-projection algorithm [17] applied on the AS-signals. The laser and the adaptive data acquisition system were automatically controlled by a PC using LabVIEW 2018 software.

Fig. 2(b) shows reconstructed images obtained for 10 different polarization angles of the excitation light for a sample (Fig. 2(a)) consisting of polarizing sheets with different orientations of optical absorption axis. It is worth noting that the conventional PACT ignores the difference of polarized light absorption by anisotropic tissues in different optical axis directions, which leads to that not every image completely shows five targets. Fig. 2(c) shows for two locations in the two respective sheets that the reconstructed image value evolves sinusoidally with polarization angle (cfr Eq. (22)), with a very high contrast between maximum and minimum absorption directions. The curves for the two locations are shifted, reflecting the different optical absorption axes of the two sheets.

In medical clinical imaging one is not interested in the direction of the maximum light absorption axis but in presenting the real image of biological tissue completely. In typical cases of samples with unknown spatial distribution of absorption magnitudes $\alpha(x,y)$ and maximum optical absorption orientations $\theta(x,y)$, we propose AP-PACT approach. For each UT position, a PA signal was recorded for each of the 10 excitation polarization angles $\varphi_1, \ldots \varphi_{10}$, as shown in Fig. 3(a). Each of the PA signals is composed of contributions originating from different regions in the uniformly excited sample, which can have different absorption values α and different maximum absorption orientation angles θ. Here, we use the σ_P as the feedback signal, calculate the σ_P of each photoacoustic response (according to Eq. (23)), and lock the median value, as shown in Fig. 3(b). Fig. 3(c) shows the median σ_P of the detector at a certain position. In view of that, our hypothesis is that the PA signal for the excitation polarization φ_* that yields the median σ_P value (among the 10 values) reflects best the overall α values across the sample. Therefore, for each of the 360 transducer orientations (in steps of 1°), the PA signal $p_d(\vec{r}_0, t_i, \varphi_*)$ that yielded the median σ_P value was kept for the image reconstruction, as shown in Fig. 3(d). From here onwards, we refer to the median $\sigma_P$value and φ_* as "adaptively selected (AS)" σ_P value and excitation polarization angle, respectively. The reconstruction result with AS-signals is shown in Fig. 3(e).

3. Experimental results

3.1. Validation on a phantom sample

In order to verify the performance of AP-PACT, we conducted an experiment on a complex phantom, consisting of two polarizing films stacked on top of each other, with an angle of about 30° between their optical axes. A photo of the phantom is shown in Fig. 4(a). Fig. 4(b) shows the optimal polarization angle (indicated by the green arrow) of incident light obtained by the UT at each scanning position using the AS-signal. Fig. 4(c) shows that, compared with images obtained with

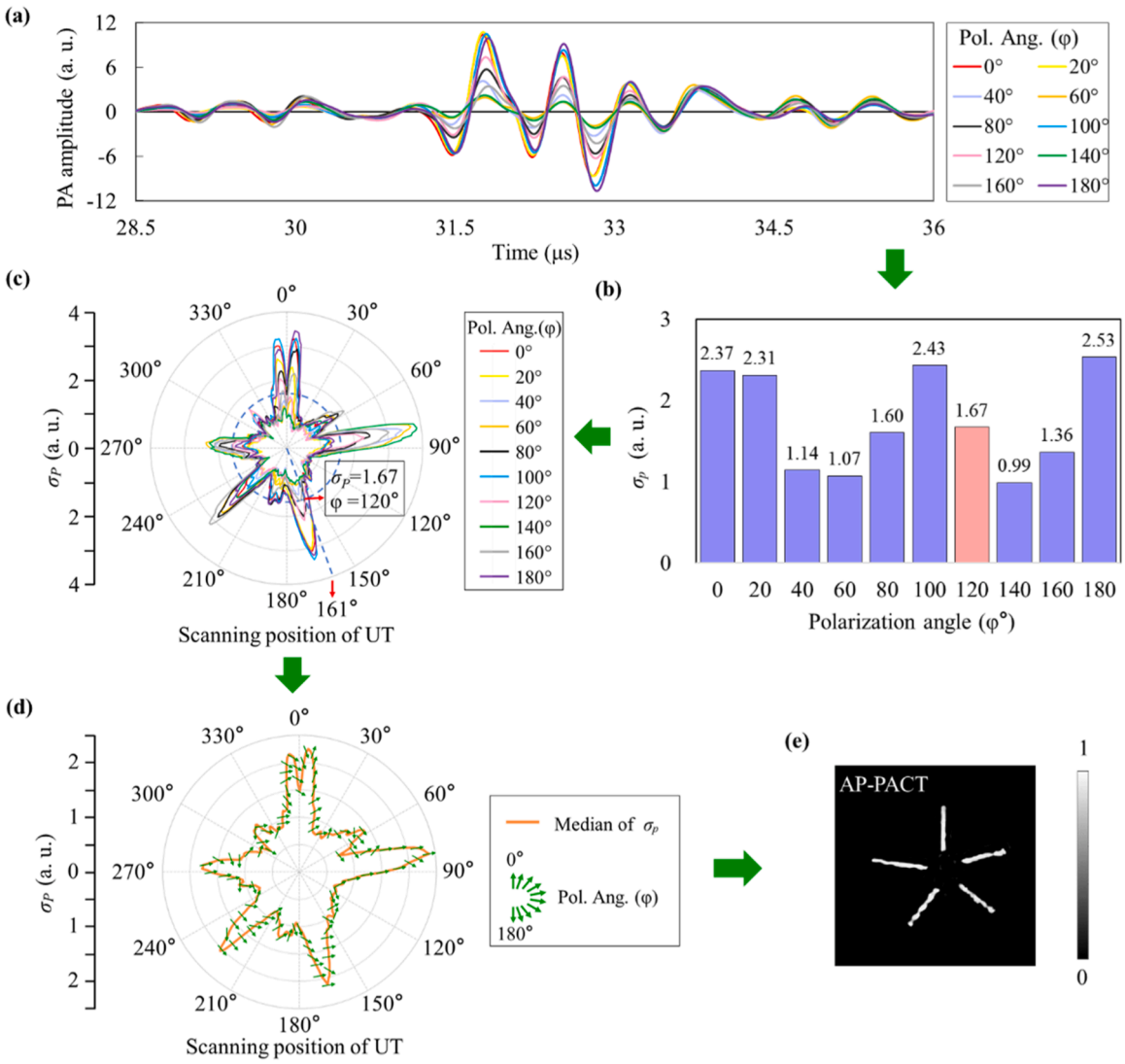

Fig. 3. Image reconstruction scheme of AP-PACT. (a) At the scanning position of 161°, a sequence of PA signal was collected by rotating the polarization of the incident light by 20°. (b) The median σ_P value of PA amplitude in (a) was calculated. (c) the σ_P of PA signal in 10 different incident-polarized light directions at each scanning position (0–360° in steps of 1°). (d) The median σ_P (orange) and its corresponding polarization direction (green arrow) of the UT at each position. (e) Reconstruction result with AS-signals (the signal corresponding to the green arrow in Fig. 3(d)).

circularly polarized light (CPACT), images obtained with the proposed AP-PACT method can make up for the lack of information and the imaging is more uniform. It is worth noting that the AP-PACT method not only improves the imaging quality but also shows an expected increase of light intensity in the region where both films are superposed. Fig. 4(d) shows the image intensity ratio for two selected positions of a single polarizer (shown by the position of B and C in Fig. 4(a)) and a superimposed polarizer (shown by the positions of A in Fig. 4(a)). Compared with CPACT, the proposed method reflects the superposition of complex sample positions more accurately.

3.2. Application on an ex-vivo sample

For an ex-vivo experiment, fresh chicken heart slices (about 15 mm in length, 16 mm in width and 3 mm in thickness) were immersed in water at 24 ℃ and subject to AP-PACT measurements, as shown in Fig. 5 (a). The green arrows in Fig. 5(b) show the AS polarization angle (φ_{**}) of the excitation light obtained for each UT orientation. Figs. 5(c) and 5(d) show the imaging results of CPACT and AP-PACT methods respectively. Compared with the results of CPACT, the image reconstructed by AP-PACT method show clearer blood vessel distribution and higher contrast. Two zoomed-in areas with abundant features of blood vessels are shown in Fig. 5(c2) and (d2) respectively. The quality of the blood vessel image of AP-PACT is better than the one obtained by CPACT, with a smoother texture and clearer features. In order to visually enhance the difference between the images obtained by the two methods, the images of Figs. 5(d1) and 5(c1) were subtracted. The resulting map is shown in Fig. 5(e1). In order to make the comparison easier, the corresponding difference was set to zero when it was lower than a certain threshold. Compared with other parts of chicken heart, the distribution of blood vessels is obviously enhanced, as shown in Fig. 5(e2). Fig. 5(f) shows a comparison of the profiles along the dotted white lines in Figs. 5(c2) and 5(d2), which indicates the AP-PACT method can improve the imaging contrast.

In a second series of ex-vivo experiments, bovine tendon slices (about 15 mm in length, 12 mm in width and 5 mm in thickness) were used. In order to get closer to a clinical scenario, optical scattering was induced. On top of the gel, we stacked an additional layer of a scattering medium (0.2 % intralipid and 2 % agar in distilled water). The bovine tendon and a vertically inserted pencil lead (with a diameter of 0.5 mm and length of 3 mm) were imaged, as shown in Fig. 6(a). Fig. 6(b) shows the optimal polarization angle (shown by the green arrow) of incident light obtained

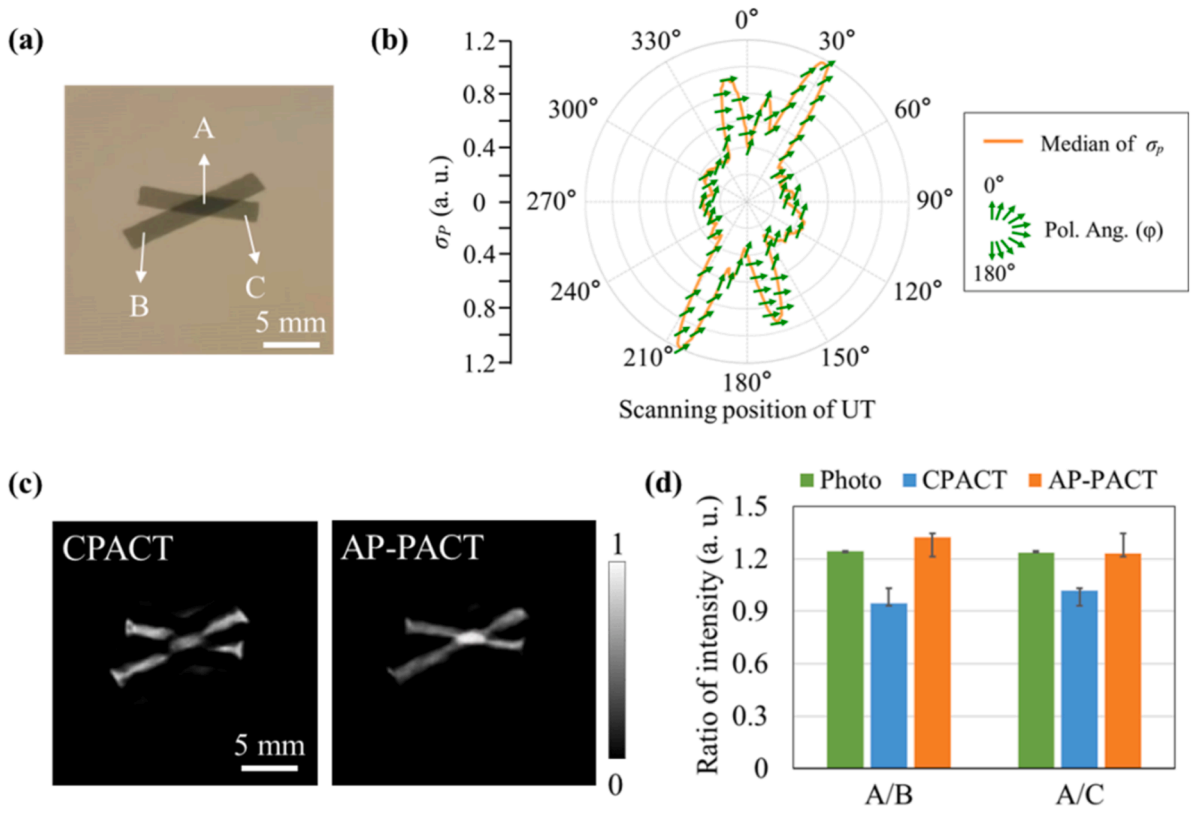

Fig. 4. Phantom imaging results. (a) Photograph of the phantom, which contains two linear polarizers overlapping each other, with 30° between their optical axes. (b) Radar plot of the median σ_P values versus UT orientation (orange). The green arrows show the direction of the polarization excitation angle for which the σ_P value. (c) Reconstruction results of the CPACT and the adaptive method AP-PACT. (d) Light intensity ratio for three selected positions (indicated in (a)), B and C are in single sheet regions and A is in a region where the 2 sheets overlap.

by the UT at each scanning position using the adaptive polarization method. Figs. 6(c) and 6(d) show the reconstruction results of the two methods. The proposed method can recover the contour information of tissue. Four zoomed-in areas are shown in Fig. 6(c2), (c3), (d2) and (d3). Comparing Figs. 6(c2) and 6(d2), it can be seen that the proposed method can make up for the beef tendon texture information [in red circles of Fig. 6(d2)]. There is little difference in pencil lead imaging, because it is isotropic, as shown in Figs. 6(c3) and 6(d3). The degree of enhancement of bovine tendon tissue at different positions is shown in Fig. 6(e): the signal magnitude is related to the angle between the polarization and the tissue fiber direction. Fig. 6(f) shows a comparison of the profiles along the dotted white lines in Figs. 6(c2) and 6(d2), which indicates the AP-PACT method can display more details of image and improve the imaging quality.

Table 1 lists three metrics for quantitative evaluation of the performance of the two methods. The standard deviation (STD) reflects the deviation of image brightness from the gray average. The larger the STD, the higher the contrast of the whole image. The root mean square gradient ($\bar{g}$) refers to the edge sharpness.

$$\mathrm{STD} = \sqrt{\frac{\sum_{i=1}^{n}(X_i - \overline{X})^2}{n-1}}. \tag{24}$$

Where X_i is the pixel value of the ith point of the image, $\overline{X}$ is the average value of all pixels of the image, and n is the number of pixels.

$$\overline{g} = \frac{1}{(m-1)(n-1)} \sum_{i=1}^{m-1} \sum_{j=1}^{n-1} \sqrt{\frac{[I(i,j) - I(i+1,j)]^2 + [I(i,j) - I(i,j+1)]^2}{2}}. \tag{25}$$

Where $I(i,j)$ represents the pixel value of the image in location (i,j).

The image entropy (H) describes how much information is provided by the image [19], and can be calculated as:

$$H = -\sum_{i=0}^{255} p_i \log p_i. \tag{26}$$

where p_i represents the proportion of pixels with pixel value i in the image.

The proposed method improves the image quality from all three aspects. The improvement of the image gradient is the most obvious: the values of bovine tendon and chicken heart images obtained by AP-PACT are almost doubled compared to CPACT.

4. Discussion and conclusion

In this work, we proposed a PACT image reconstruction technique, AP-PACT, that made use of polarization adaptation of the excitation light, in an effort aimed at mitigating effects of PA image distortion due to spatially inhomogeneous anisotropic absorption of tissues, which occurs in conventional PACT. Compared with the recently proposed approaches, we focused on obtaining the polarization-dependent signals to compensate for the loss information of anisotropic tissue imaging. At the same time, the theoretical relationship between polarized light angle and tissue optical absorption in the field of PA imaging is perfected.

In view of having a robust interpretation of PA images obtained for given excitation light polarizations in materials with anisotropic optical absorption properties, first, the relationship between light absorption and the polarization angle with the excitation light was deduced. Next, a new approach was elaborated to improve the imaging quality of anisotropic biological tissues in a photoacoustic configuration that made use of PA signals obtained by an ultrasound transducer that scanned the

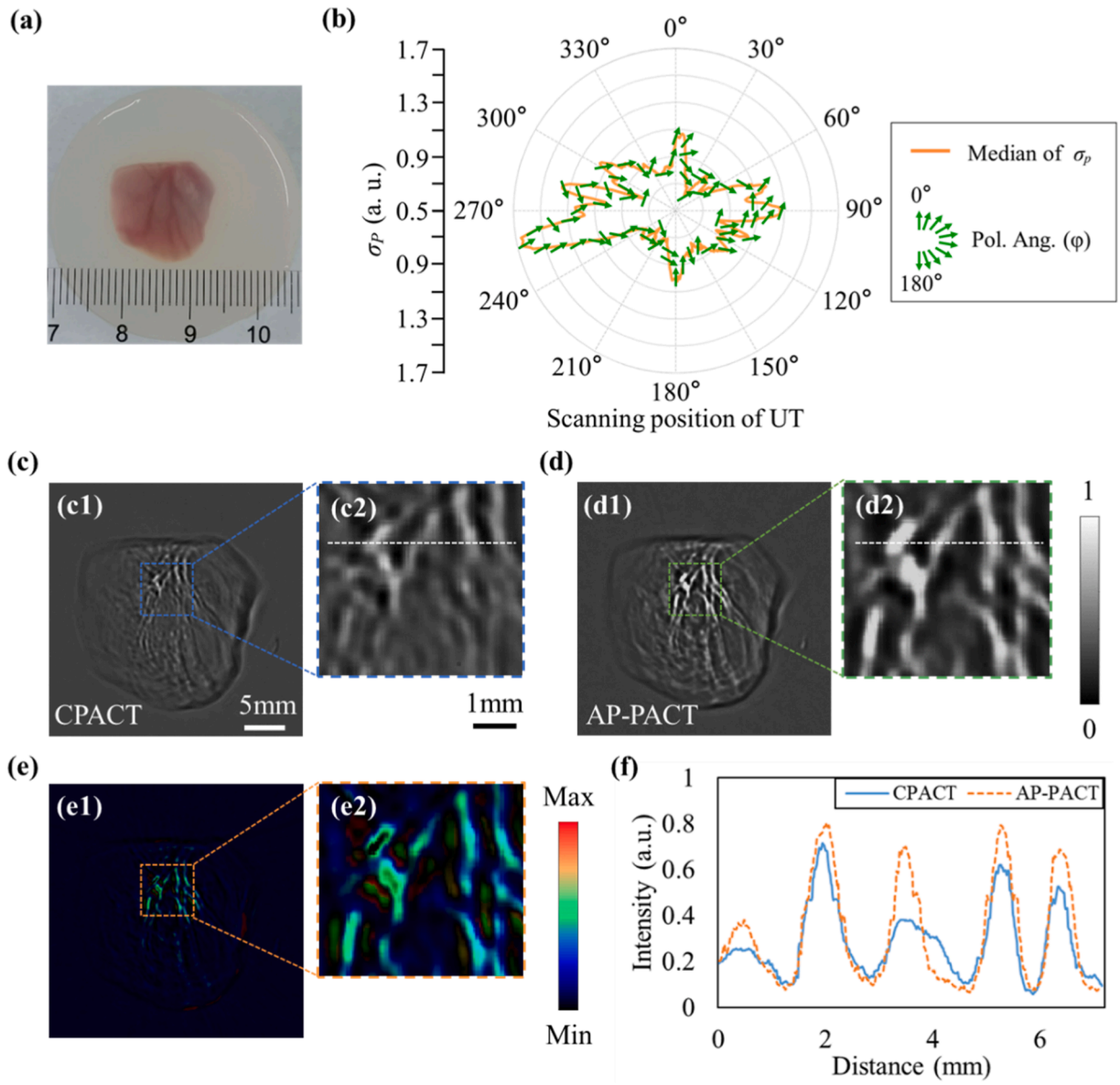

Fig. 5. Imaging results of ex-vivo chicken heart. (a) Photograph of the sample. (b) Radar plot of AS σ_P values of excitation light at each scanning position of the UT. (c)–(d) are the reconstructed results of the proposed AP-PACT and the CPACT, respectively. (c2)–(d2) Zoomed-in views of the regions in colored dashed boxes in (c1) and (d1). (e1) Thresholded difference between images (d1) and (c1). (f) The comparison of the profiles along the dotted white lines in (c2) and (d2).

region of interest along a circle. Considering the depolarization of polarized light in tissue transmission, for each ultrasonic transducer orientation, the σ_P value of PA signals obtained for different excitation polarizations was determined and the PA signal that yielded the median σ_P value was retained for the image reconstruction. The idea was that these selected PA signals were least affected by extreme absorption values, and thus were also least affected by inhomogeneous absorption anisotropy.

Experiments on strongly anisotropic model samples confirm that the polarization direction of the incident light affects the image quality in conventional PACT, and that the AP-PACT method is effectively improving the quality.

As a newly developed reconstruction method, the ability of AP-PACT is yet to be further developed and improved. In future research, other parameters than the $\sigma_P$value of the PA signals could be used to select or combine PA signals obtained for different excitation polarizations. In view of possible in-*vivo* biological imaging, further acceleration of the imaging could be achieved by replacing the scanning transducer by a ring array of transducers. In addition, the change of cell polarity is a sign of cancer [20], and conventional optical polarization imaging can not penetrate deep tissue for imaging. In the future, AP-PACT may bring new possibilities for early clinical detection of bone cancer [21].

Declaration of Competing Interest

We declare that we have no financial and personal relationships with other people or organizations that can inappropriately influence our work, there is no professional or other personal interest of any nature or kind in any product, service and/or company that could be construed as influencing the position presented in, or the review of, the manuscript entitled, “Adaptive polarization photoacoustic computed tomography for biological anisotropic tissue imaging.”

Data Availability

Data will be made available on request.

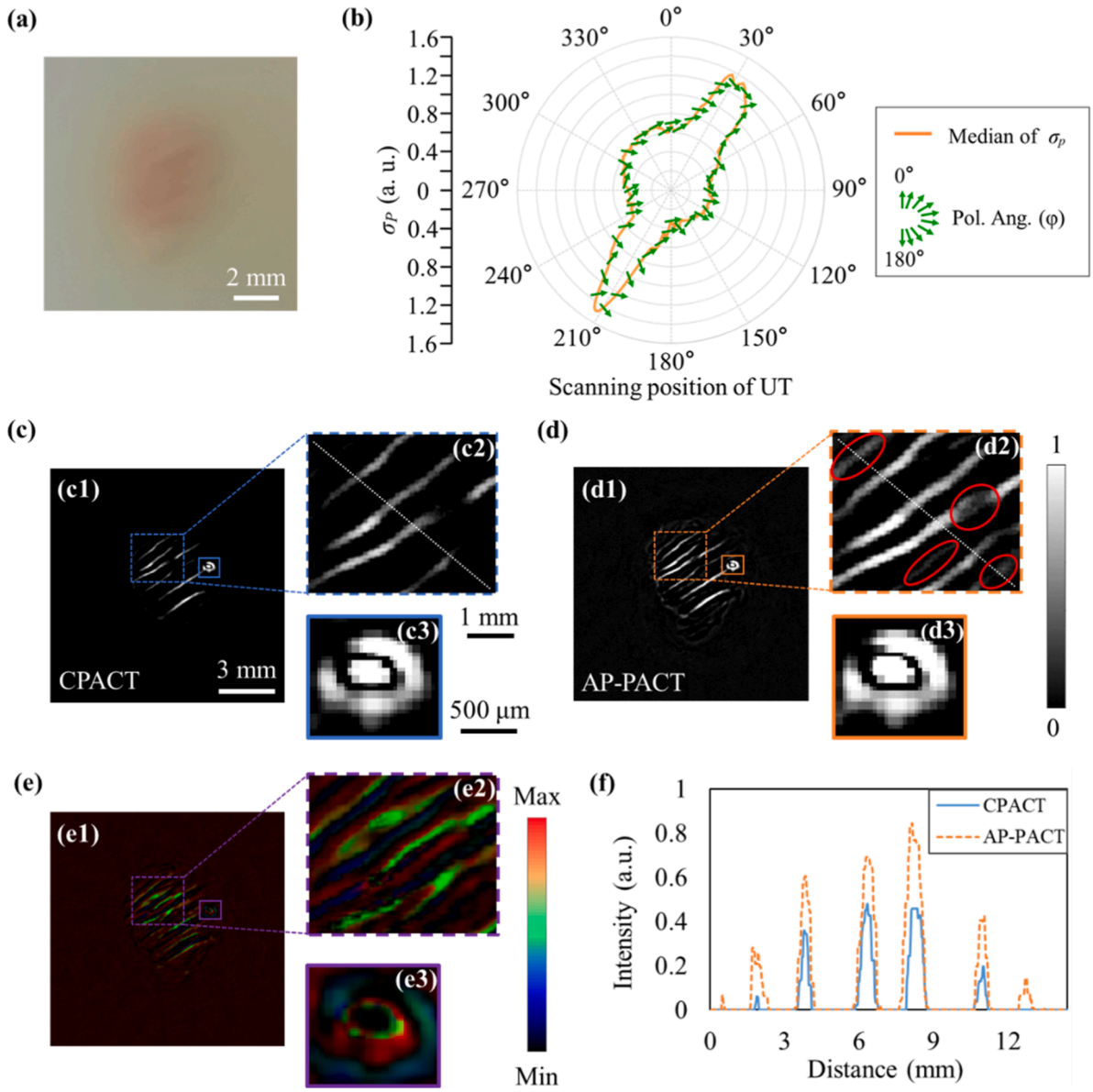

Fig. 6. Imaging results of bovine tendon. (a) Photograph of bovine tendon samples. (b) AS polarization direction of incident light at each scanning position of the UT. (c)–(d) Reconstructed results of the CPACT and the proposed method, respectively. (c2)–(d2) Zoomed-in views of the regions in colored dashed boxes in (c1) and (d1). (c3)–(d3) Zoomed-in views of the regions in colored solid boxes in (c1) and (d1). (e1) Difference between (c1) and (d1) images. (e2) and (e3) Zoomed-in views of the regions in the colored dashed box and solid box in (e1), respectively. (f) The comparison of the profiles along the dotted white lines in (c2) and (d2).

Table 1
Quantitative evaluation of different methods in ex-vivo experiments, based on the standard deviation (STD), the gradient ($\bar{g}$) and the entropy (H).

Imaging mode	STD		$\bar{g}$		H	
Phantom	CPACT	AP-PACT	CPACT	AP-PACT	CPACT	AP-PACT
Bovine tendon	13.024	**16.695**	0.009	**0.017**	3.702	**4.760**
Chicken heart	11.795	**18.348**	0.012	**0.022**	4.850	**5.534**

Acknowledgments

This research was supported by National Key Scientific Instrument and Equipment Development Projects of China (61827814); Natural Science Foundation of Beijing Municipality (Z190018); Overseas Expertise Introduction Project for Discipline Innovation of China (B17023). The authors would also like to acknowledge support from the UK Engineering and Physical Sciences Research Council (EP/R042578/1).

Appendix A. Supporting information

Supplementary data associated with this article can be found in the online version at doi:10.1016/j.pacs.2023.100543.

References

[1] L.V. Wang, S. Hu, Photoacoustic tomography: in vivo imaging from organelles to organs, Science 335 (6075) (2012) 1458–1462.
[2] S. Zackrisson, S.M.W.Y. van de Ven, S.S. Gambhir, Light in and sound out: emerging translational strategies for photoacoustic imaging, Cancer Res. 74 (4) (2014) 979–1004.
[3] A. Taruttis, V. Ntziachristos, Advances in real-time multispectral optoacoustic imaging and its applications, Nat. Photonics 9 (4) (2015) 219–227.

[4] S. Alali, Y.T. Wang, I.A. Vitkin, Detecting axial heterogeneity of birefringence in layered turbid media using polarized light imaging, Biomed. Opt. Express 3 (2012) 3250–3263.
[5] V.V. Volkov, V.B. Loshchenov, V.I. Konov, V.V. Kononenko, Fibreoptic diffuse-light irradiators of biological tissues, Quantum Electron. 40 (8) (2010) 746–750.
[6] S.L. Jacques, Optical properties of biological tissues: a review, Phys. Med. Biol. 58 (2013) R37–R61.
[7] S. Jana, S.K.L. Levengood, M. Zhang, Anisotropic materials for skeletal-muscle-tissue engineering, Adv. Mater. 28 (48) (2016) 10588–10612.
[8] A. Kienle, F.K. Forster, R. Diebolder, R. Hibst, Light propagation in dentin: influence of microstructure on anisotropy, Phys. Med. Biol. 48 (2) (2003) 7–14.
[9] S. Vilov, G. Godefroy, B. Arnal, E. Bossy, Photoacoustic fluctuation imaging: theory and application to blood flow imaging, Optica 7 (2020) 1495–1505.
[10] V.V. Tuchin, Polarized light interaction with tissues, J. Biomed. Opt. 21 (7) (2016), 071114.
[11] C. He, H. He, J. Chang, B. Chen, H. Ma, M.J. Booth, Polarisation optics for biomedical and clinical applications: a review, Light Sci. Appl. 10 (2021) 194.
[12] D. Razansky, C. Vinegoni, V. Ntziachristos, Polarization-sensitive optoacoustic tomography of optically diffuse tissues, Opt. Lett. 33 (20) (2008) 2308–2310.
[13] Y. Qu, L. Li, Y.C. Shen, X.M. Wei, T.T.W. Wong, P. Hu, J.J. Yao, K. Maslov, L. V. Wang, Dichroism-sensitive photoacoustic computed tomography, Optica 5 (4) (2018) 495–501.
[14] S. Hu, K. Maslov, P. Yan, J.M. Lee, L.V. Wang, Dichroism optical-resolution photoacoustic microscopy, Proc. SPIE Int. Soc. Opt. Eng. 8223 (2012).
[15] Z. Zhang, Y. Shi, L. Xiang, D. Xing, Polarized photoacoustic microscopy for vectorial-absorption-based anisotropy detection, Opt. Lett. 43 (21) (2018) 5267–5270.
[16] Y. Zhou, J. Chen, C. Liu, C. Liu, P. Lai, L. Wang, Single-shot linear dichroism optical-resolution photoacoustic microscopy, Photoacoustics (2019), 100148.
[17] Y. Zhou, J. Yao, L.V. Wang, Tutorial on photoacoustic tomography, J. Biomed. Opt. 21 (6) (2016), 061007.
[18] Y. Zhang, S.F. Yang, Z.Y. Xia, R.J. Hou, B. Xu, L.P. Hou, J.H. Marsh, J.J. Hou, S.M. R. Sani, X.F. Liu, J.C. Xiong, Co-optimization method to improve lateral resolution in photoacoustic computed tomography, Biomed. Opt. Express 13 (9) (2022) 4621–4636.
[19] D.Y. Tsai, Y. Lee, E. Matsuyama, Information entropy measure for evaluation of image quality, J. Digit. Imaging 21 (3) (2008) 338–347.
[20] M. Lee, V. Vasioukhin, Cell polarity and cancer-cell and tissue polarity as a non-canonical tumor suppressor, J. Cell Sci. 121 (2008) 1141–1150.
[21] S. Jana, S.K.L. Levengood, M. Zhang, Anisotropic materials for skeletal-muscle-tissue engineering, Adv. Mater. 28 (48) (2016) 10588–10612.

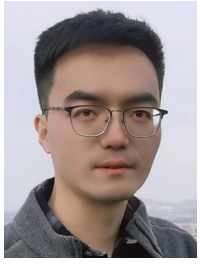

Yang Zhang is a Ph.D. student majoring in Optical Engineering from Nanjing University of Science and Technology, Nanjing, China. He received his M.S. degree in Control Engineering from Kunming University of Science and Technology, Kunming, China in 2018. His current research interests are photoacoustic computed tomography, image reconstruction algorithm and application in clinical disease detection.

Christ Glorieux obtained his Ph.D. degree in 1994 at the Physics and Astronomy department of KU Leuven, Belgium. He is active in research and teaching physics and sounds and waves, electromagnetism, optics and experimental physics to undergraduate and graduate students. He is leading a research team in the field of photothermal and photoacoustic applications for the fundamental study of the thermophysical properties of complex soft, biological and heterogeneous matter, the development of measurement techniques in acoustics and optics and for the characterization and depth profiling of thin (sub-micron) layered structures, with applications in the field of non-destructive testing.

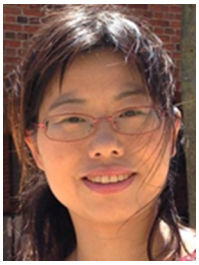

Shufan Yang is the Associate Professor in Computational Intelligence, at School of Computing, Engineering and Build Environment, Edinburgh Napier University. Before joining Napier, she was a lecturer at the University of Glasgow and the University of Wolverhampton. She completed her Ph.D. at the Advanced Processor Technologies Group (2006–2010) at the University of Manchester. Her current research interests include biomedical imaging, computer-aided diagnosis, deep learning, computer vision, medical computing and health informatics.

Kai Gu is now studying for a Ph.D. in the School of Electronic and Optical Engineering, Nanjing University of Science and Technology, Nanjing, China. His research interests are polarized light propagation in tissues and surface plasmon polariton.

Zhiying Xia graduated in opto-electronics information science and engineering from Nanjing University of Science and Technology (NJUST) in 2017. She is a Ph.D. student majoring in Optical Engineering from NJUST, Nanjing, China. Her research focus on photoacoustic microscopy imaging, acoustic vibrations and acousto-plasmonics.

Ruijie Hou is a Ph.D. student majoring in Optical Engineering from Nanjing University of Science and Technology, Nanjing, China. Her research interests are photoacoustic generation and wavefront shaping.

Lianping Hou received his Ph.D. degree from the Institute of Semiconductors (IOS), Chinese Academy of Sciences (CAS), and was the sole winner of the 2005 Baosteel Scholarship of IOS-CAS. He is currently a Reader at the James Watt School of Engineering, University of Glasgow (UOG), focusing on high frequency and high power semiconductor mode-locked lasers and integrated optoelectronics. He is a senior IEEE member, an Associate Editor of Electronics Letters, Editor of American Journal of Modern Physics, Photonics. He has published over 190 journal and conference papers and currently holds several patents.

Xuefeng Liu received his Ph.D. degree in 1993 at The University of Sheffield. He is currently a Zijin Distinguished Professor in the School of Electronic and Optical Engineering, Nanjing University of Science and Technology, Nanjing, China. He created the research field of super-resolution imaging, photon state parametric indirect microscopic imaging (PIMI), theory and instrumentation. He is an expert in photoacoustic imaging, optical super-resolution imaging and photonic healthcare diagnosis. He has published over 60 academic articles.

Jichuan Xiong received his M.S. degree in Optical Engineering from Southwest Institute of Technical Physics, Chengdu, China in 2008, and the Ph.D. degree in Physics from KU Leuven, Belgium in 2013. He is currently an associate professor in the School of Electronic and Optical Engineering, Nanjing University of Science and Technology, Nanjing, China. He has published about 30 journal papers on top journals, such as Nanophotonics, ACS Photonics, Nanoscale Adv., OL, OE, BOE, IEEE Photon. J. and so on. His research interests include photoacoustic imaging for biomedical applications, optical super-resolution imaging, laser ultrasonic non-destructive techniques and instrumentation.